Age-dependent alterations in the head-direction signal in a rat model of Fragile X Syndrome

Noah Moore[1*], Adrian J. Duszkiewicz[2*], Antonis Asiminas[1,3], Paul A. Dudchenko[2], Adrien Peyrache[4**], Emma R. Wood[1**]

[1]Centre for Discovery Brain Sciences & Simons Initiative for the Developing Brain, University of Edinburgh, Edinburgh, UK;
[2]Division of Psychology, University of Stirling, Stirling, UK
[3]Center for Translational Neuromedicine, University of Copenhagen, Copenhagen, Denmark.
[4]Montreal Neurological Institute and Hospital, McGill University, Montreal, Canada;
* Equal contribution
** Corresponding authors

Abstract

Fragile X Syndrome (FXS) is a common monogenic cause of autism spectrum disorder and intellectual disability (ASD/ID), but the neural mechanisms underlying its symptoms remain unclear. Here, we investigate the development of the head-direction (HD) system in a rat model of FXS (*Fmr1*$^{-/y}$ rats). Using high-density silicon probes, we recorded neuronal activity in the postsubiculum (PoSub), a cortical hub of the HD system, during exploration and sleep in juvenile and adult *Fmr1*$^{-/y}$ and wild-type (WT) rats. Juvenile *Fmr1*$^{-/y}$ rats exhibited enhanced HD tuning characterized by sharper directional tuning curves and improved stability of the HD signal in relation to the external environment. This enhancement was intrinsic to the HD circuit and persisted across behavioral and sleep states. However, by adulthood, HD tuning in *Fmr1*$^{-/y}$ rats became unstable, with increased drift in the allocentric reference frame despite intact intrinsic HD dynamics. These findings reveal a transient enhancement of spatial coding in the HD system of juvenile *Fmr1*$^{-/y}$ rats, followed by a degradation in adulthood, providing insights into network-level dysfunctions in FXS and their developmental trajectories. Overall, our work establishes the HD system as a valuable and tractable model for studying neurodevelopmental disorders.

Introduction

Autism spectrum disorder and intellectual disability (ASD/ID) are comorbid conditions characterized by abnormalities in early cognitive development that persist into adulthood. In many cases, their symptoms are linked to *de novo* or inherited mutations in genes involved in neuronal function [1]. With the aid of genetic rodent models, much progress has been made in uncovering how these single-gene mutations affect intracellular processes like excitability, synaptic transmission and plasticity [2]. Still, cognition rises from the orchestrated activity of large neural populations, but how such intracellular phenotypes affect the way neuronal ensembles represent the external world is not well understood. This knowledge gap arises from the need to interpret the activity of cognitive circuits in behaving animals early in postnatal development - a task aided by the recent introduction of various rat ASD/ID models [3–8]. Indeed, compensation mechanisms that emerge throughout adolescence often occlude the primary circuit dysfunctions that give rise to ASD/ID phenotypes [9]. In recent years, the problem has been addressed by focusing on primary

sensory systems [10–12], in which neural tuning to sensory features can be quantified even in early postnatal development [13–15]. However, neural activity in sensory systems is principally driven by external stimuli and is thus sensitive to aberrations in upstream sensory processing as well as attentional control, each of which may also be affected in ASD/ID [16,17]. Altogether, this highlights the need to develop new paradigms to accurately assess the functional properties of cognitive circuits in juvenile rat models of ASD/ID, both when such activity is driven by and independent of external stimuli and attentional control.

In contrast to primary sensory systems, neurons in cortical networks that give rise to the brain's cognitive map often exhibit narrow tuning related to the animal's current position or direction in space [18]. This spatial selectivity enables detailed mapping of their receptive fields in juvenile rodents engaged in simple spatial exploration [19–22]. Importantly, neural activity in these networks is often constrained on low-dimensional neural manifolds that persist across wakefulness (the 'online' state') and sleep (i.e. the 'offline' state') [23–26]. Recent work has shown that such manifolds provide access to neuronal tuning independently of the stimulus space [23,24,27,28], which makes them ideal candidate model systems to study early postnatal network development *in vivo*.

The rodent head-direction (HD) circuit is a canonical example of a network in which population activity invariantly represents a one-dimensional circular variable [23,29]. It consists of HD cells, which each fire when the animal faces a particular direction, independently of its location and behaviour [30,31]. In an online state, the combined activity of HD cells corresponds to the animal's current HD in the allocentric reference frame, while in offline states it no longer relates to the external world and instead represents an internally-generated and drifting 'virtual HD' [23,29]. Thus, the signal encoded by the HD system can be probed even during offline states, without the confounding influence of sensory or attentional processing.

Here, we characterized HD coding across juvenile development in a rat model of Fragile X Syndrome (FXS), a common monogenic cause of ASD/ID, which is caused by lack of a functional *FMR1* gene [32]. *FMR1* encodes the Fragile X messenger ribonucleoprotein (FMRP), a brain-enriched mRNA binding protein that regulates protein translation. We found that the cortical HD signal in male rats lacking FMRP (*Fmr1*$^{-/y}$ rats) is enhanced early in postnatal development but becomes unstable by adulthood. Using manifold analysis across online and offline brain states, we establish that the juvenile enhancement is largely due to differences in intrinsic dynamics, while deterioration during adulthood stems from the difficulty with anchoring the HD signal to the external world. Overall, we introduce the rodent HD circuit as a valid and tractable model system that allows for unprecedented insights into network-level phenotypes in rodent models of neurodevelopmental disorders.

Results

To compare HD cell tuning in juvenile wild-type (WT) and *Fmr1*$^{-/y}$ rats, we recorded populations of neurons in the postsubiculum (PoSub), the cortical hub of the HD system, in juvenile (P22-28) male *Fmr1*$^{-/y}$ rats and WT littermates using high-density silicon probes (Figure 1a). PoSub cell activity was recorded while rats foraged for scattered cereal in a cylindrical open field (Figure S1a) for two 20 min sessions separated by a 90 min period of rest, during which sleep activity was recorded. Juvenile *Fmr1*$^{-/y}$ rats showed no differences in exploratory behaviour in comparison with their WT littermates (Figure S1b-c).

We recorded 406 units from 7 WT rats and 372 units from 5 *Fmr1*$^{-/y}$ rats. Excitatory cells in PoSub tend to be robustly tuned to HD in both adult and post-weaning juvenile rats [21,22,30], so we limited our analysis to this putative cell type, using trough-to-peak duration as the classification criterion (range: 8-83 putative excitatory units per recording; Figure S1e). To account for both inter- and intra-animal variability, statistical significance of cell-level data was assessed using linear mixed effects (LME) modelling with genotype as the fixed factor, and animal and cell as random factors [33].

We observed that many putative excitatory cells in PoSub (henceforth referred to as PoSub cells) in WT juvenile rats had directional tuning curves, but these were often not well-defined (Figure 1b-d), In contrast, to our surprise, PoSub cells in juvenile *Fmr1*$^{-/y}$ rats often exhibited robust tuning to HD (Figure 1b-d). Quantification of HD tuning using either HD information (HD info) or the width of the tuning curves (Figure 1e-f) confirmed that overall PoSub cells in juvenile *Fmr1*$^{-/y}$ rats were more sharply tuned to HD than PoSub cells in their WT littermates. This difference in tuning was not associated with differences in cluster quality (Figure S1f), firing rates (Figure S1g-h) or electrode positions (Figure S1d).

The unusually narrow HD tuning curves in juvenile *Fmr1*$^{-/y}$ rats could be explained either by improved anchoring of the HD signal to the external world or by intrinsically enhanced HD tuning. We thus first quantified the stability of HD tuning within each recording session. The overall magnitude of HD tuning was stable across the recording (Figure 1g, FigureS1j), but HD receptive fields in juvenile *Fmr1*$^{-/y}$ rats drifted less than those of WT rats with respect to the allocentric reference frame of the open field within individual sessions (Figure 1h), despite no difference in overall drift between recording sessions (Figure S1k). This improved anchoring of the HD signal to the external world in juvenile *Fmr1*$^{-/y}$ rats was further confirmed on the population level via Bayesian decoding (Figure 1i-j). Thus, the apparent enhancement of HD tuning in juvenile *Fmr1*$^{-/y}$ rats could be partially explained by lower drift of the HD signal with respect to the allocentric reference frame.

WT rats if computed independently of the allocentric reference frame. In other words, the fidelity of the internally generated HD signal (the 'virtual HD') should be the same between the two groups, and should only differ in how this internal HD signal relates to the animal's real HD. Highly structured intrinsic dynamics within the HD circuit enable estimation of relative HD tuning curves from population activity alone, independently of any external variables and reference frames [23,34]. We thus applied the Isomap dimensionality reduction technique to the PoSub cell population vectors obtained during the exploration sessions. In both WT and *Fmr1*$^{-/y}$ juvenile rats, the angular coordinate of population activity projected onto two dimensions corresponded to the animal's current HD and could be used to compute intrinsic ('Isomap') HD tuning curves (Figure 2a-b). Overall, Isomap tuning curves corresponded well to the HD tuning curves calculated in the allocentric reference frame (Figure 2c). However, while HD tuning curves in WT rats showed signs of drift, Isomap tuning curves were not contaminated by drift with respect to the external world since they were based on the internal representation of HD. To our surprise, these intrinsic Isomap tuning curves were better HD-tuned in juvenile *Fmr1*$^{-/y}$ rats than in their WT littermates (Figure 2d). Thus, PoSub cells in juvenile *Fmr1*$^{-/y}$ rats exhibited intrinsically enhanced tuning to HD independently of the differences in anchoring to the external world

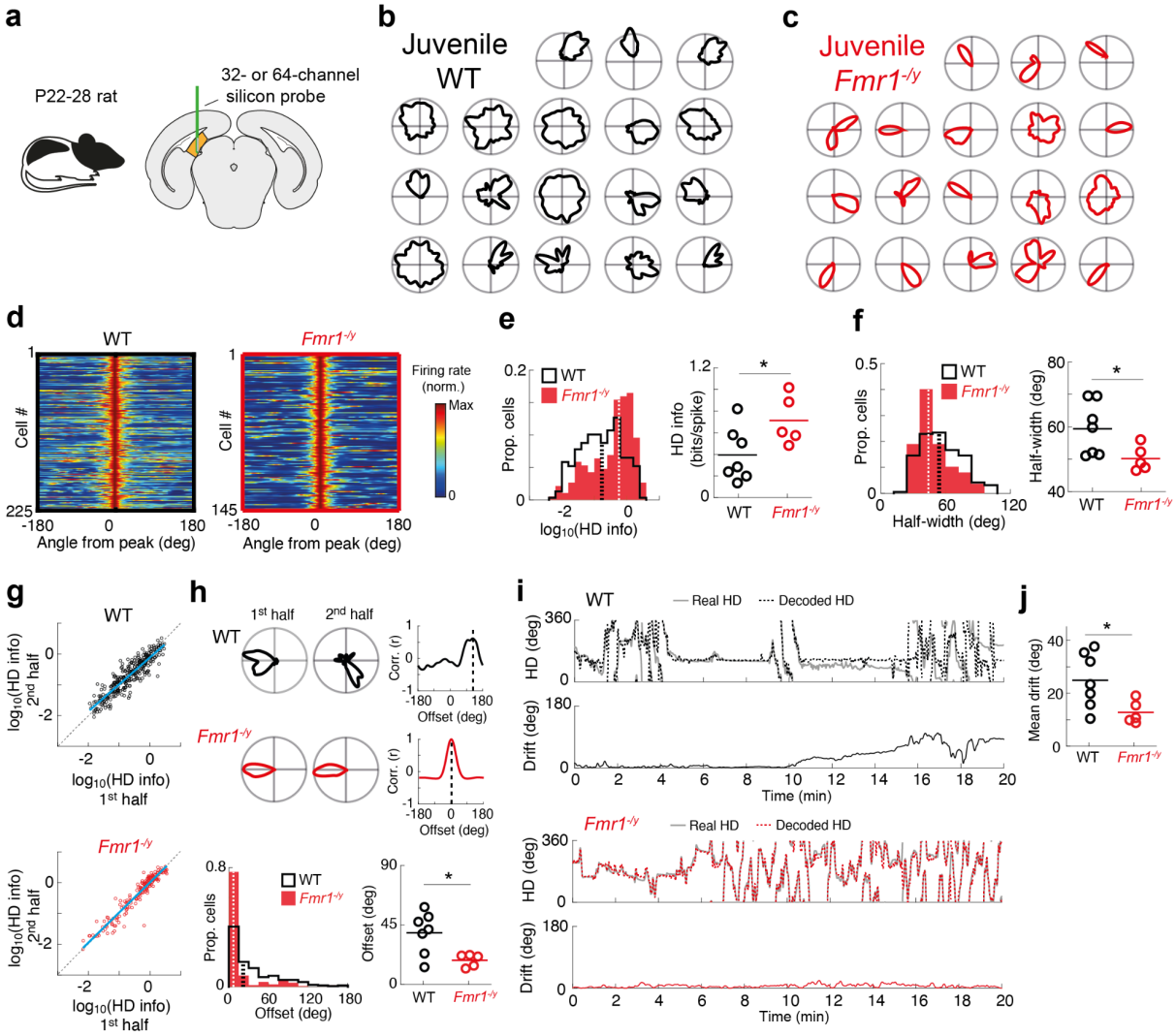

Figure 1. Enhanced HD tuning and HD signal stability in juvenile *Fmr1*$^{-/y}$ rats. a, silicon probe placement in PoSub. **b**,**c**, example tuning curves of PoSub cells in juvenile WT rats (**b**) and juvenile *Fmr1*$^{-/y}$ rats (**c**). **d**, normalized HD tuning curves of PoSub cells with tuning curve width of less than 120 degrees. **e**, **f**, overall distribution (left) and animal averages (right) of HD info (**e**) and tuning curve width (**f**) indicate enhanced HD tuning in juvenile *Fmr1*$^{-/y}$ rats (HD info, LME: genotype effect, $P < 0.05$; half-width, LME: genotype effect, $P < 0.05$). **g**, Relationship between HD tuning of PoSub cells across two halves of the exploration epoch (WT, $r = 0.90$, $P < 10^{-118}$; *Fmr1*$^{-/y}$, $r = 0.95$, $P < 10^{-123}$). Blue lines, linear fits. **h**, top, examples of HD tuning curves for two halves of a recording epoch and associated tuning cross-correlograms, showing considerable drift in a PoSub cell from a WT rat but a stable firing direction in a cell from an *Fmr1*$^{-/y}$ rat. Dashed lines, angular offset of maximum tuning curve correlation. Bottom, distribution and animal averages of tuning curve offsets between two halves of the exploration epoch, indicating enhanced anchoring of the HD signal to the allocentric reference frame in *Fmr1*$^{-/y}$ rats (angular offset between tuning curves, LME: genotype effect, $P < 0.05$). **i**, example real and decoded HD during a single recording session in WT and *Fmr1*$^{-/y}$ rats, as well as the drift of the decoded HD with respect to the animal's real HD. **j**, average drift of the HD signal across all recording sessions (t-test on animal averages: $t(10) = 2.44$, $P < 0.05$). Dashed lines on histograms, population medians; horizontal lines on animal average panels, means of animal averages.

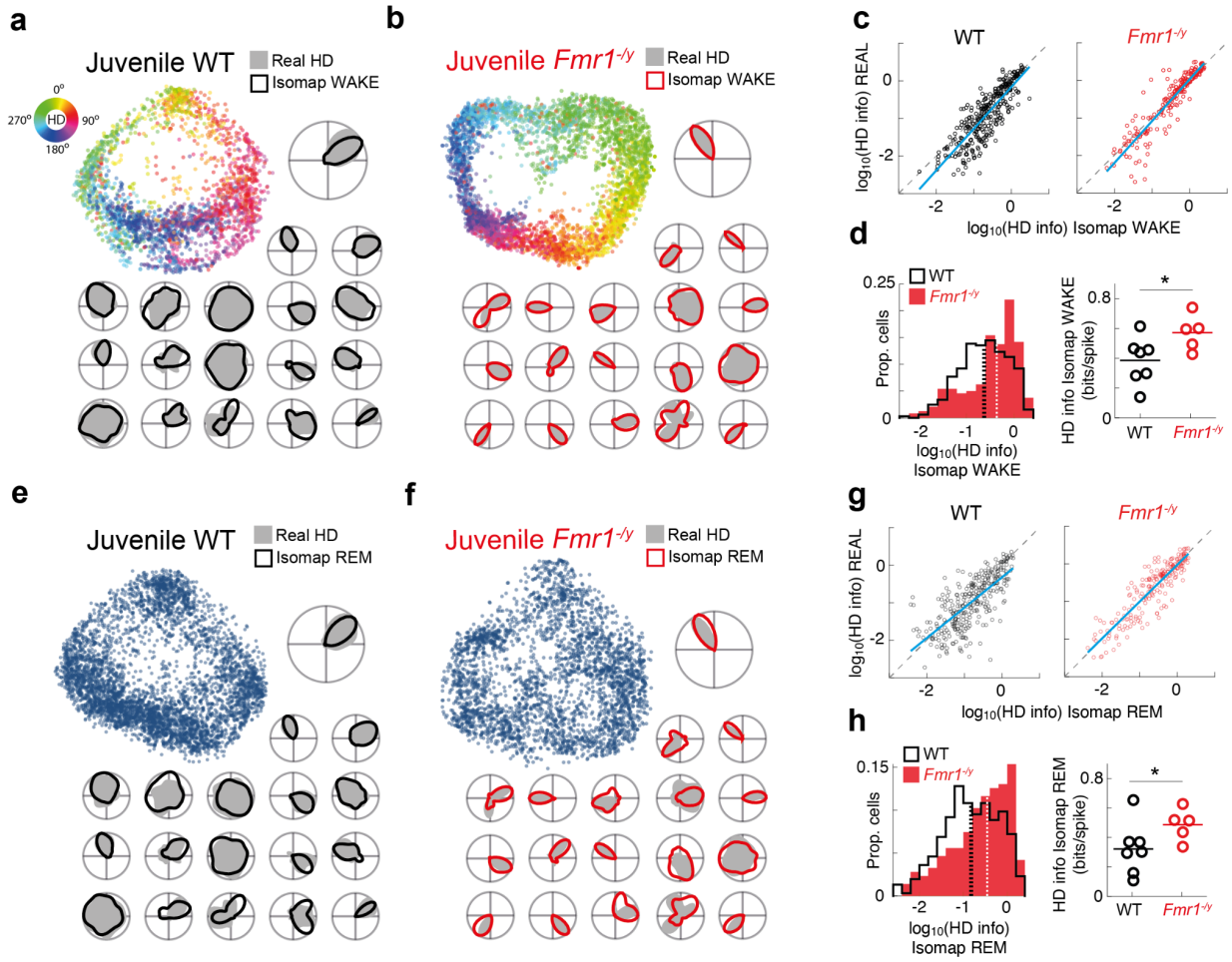

Figure 2. PoSub cells in juvenile *Fmr1*$^{-/y}$ rats show enhanced tuning to the internally generated HD signal. **a**, **b**, Examples of Isomap projections of PoSub cell population vectors during a single awake exploration session (WAKE) in a juvenile WT rat (**a**) and an *Fmr1*$^{-/y}$ rat (**b**), with each population vector colored according to the animal's current HD, as well as HD tuning curves computed in the allocentric reference frame (real HD) and reconstructed using the angle from the centre of the manifold (Isomap WAKE). The mapping of real HD onto the manifold is more diffuse in WT rats, indicating drift of the internal HD with respect to the allocentric reference frame. **c**, Magnitude of HD tuning in PoSub cells is preserved in the tuning curves reconstructed only from population activity during WAKE (WT, $r = 0.84$, $P < 10^{-88}$; *Fmr1*$^{-/y}$, $r = 0.92$, $P < 10^{-101}$). Blue lines, linear fits. **d**, overall distribution (left) and animal averages (right) of HD info indicate enhanced HD tuning in juvenile *Fmr1*$^{-/y}$ rats when measured independently of any reference frames (LME: genotype effect, $P < 0.05$). **e**, **f**, Examples of Isomap projections of PoSub population vectors during REM sleep from the same recording session as in **a** and **b**. HD tuning curves can be reliably reconstructed from the REM activity alone (Isomap REM), in the absence of consciousness (i.e. offline). **g**, Magnitude of HD tuning in PoSub cells is preserved in the Isomap REM tuning curves in both genotypes (WT, $r = 0.73$, $P < 10^{-50}$; *Fmr1*$^{-/y}$, $r = 0.90$, $P < 10^{-76}$). Blue lines, linear fits. **h**, overall distribution (left) and animal averages (right) of HD info indicate enhanced HD tuning in juvenile *Fmr1*$^{-/y}$ rats even when measured from internally generated activity during REM (LME: genotype effect, $P < 0.05$). Dashed lines on histograms, population medians; horizontal lines on animal average panels, means of animal averages.

If the differences in anchoring to the external world are indeed underlying the apparent differences in HD tuning, we would expect the overall HD tuning in juvenile *Fmr1*$^{-/y}$ rats to be similar to that in

While virtual HD obtained from population activity during wake periods should be independent of drift, it is still conceivable that it is to some degree influenced by ongoing behaviour. In contrast, population activity during sleep is internally generated and governed only by internal dynamics. We thus took advantage of the fact that HD cell population dynamics during Rapid Eye Movement (REM) sleep are virtually indistinguishable from wakefulness, with the HD signal drifting around at real-time speed despite the animal being stationary [23,25,26,29]. This virtual HD can be reliably decoded from HD cell population activity during REM, and HD tuning curves can be reconstructed purely from internally generated activity in "offline" states (Figure 2e-f). Similar to wakefulness, Isomap tuning curves generated from REM population activity corresponded well to the HD tuning curves calculated in the allocentric reference frame during exploration but were free from drift (Figure 2e-g). Importantly, PoSub cells in juvenile *Fmr1*$^{-/y}$ rats still showed enhanced HD tuning relative to that of WT rats even when the tuning was computed from internally generated activity during REM sleep (Figure 2h). Overall, these findings indicate that in addition to enhanced anchoring to the allocentric reference frame, HD tuning in juvenile *Fmr1*$^{-/y}$ rats is intrinsically more precise.

We then sought to establish whether this surprising enhancement in the fidelity of cortical HD signal in juvenile *Fmr1*$^{-/y}$ rats is transient or persists to adulthood. To that end, we recorded PoSub activity in adult *Fmr1*$^{-/y}$ rats (n = 507 units from 6 rats) and WT littermates (n = 543 units from 6 rats) in the same experimental protocol (range: 30-114 putative excitatory units per recording; Figure 3a, Figure S2a-d). While HD tuning in adult *Fmr1*$^{-/y}$ rats often appeared slightly less smooth than in WT rats (Figure 3b-d), overall there were no significant differences in the tuning to HD between the groups (Figure 3e-f; Figure S2e-j). Interestingly, while juvenile *Fmr1*$^{-/y}$ rats exhibited superior anchoring of the HD signal to the external world, adult *Fmr1*$^{-/y}$ rats showed the opposite effect, with stronger drift of the HD signal both within individual sessions (Figure 3g-j) and between the two recording epochs conducted 90 min apart (Figure S2k). Consistent with the similar HD tuning between genotypes, there were no differences in the tuning of Isomap HD tuning curves obtained during wakefulness (Figure 4a-d) or REM sleep (Figure 4e-h) between adult WT and *Fmr1*$^{-/y}$ rats. Thus, the enhancement in the quality of the intrinsic HD receptive fields in juvenile *Fmr1*$^{-/y}$ rats is only transient and disappears as the rats reach adulthood. Furthermore, the superior anchoring of the HD signal to the external world observed in juvenile *Fmr1*$^{-/y}$ rats seems to degrade in adulthood, resulting in significant drift of the HD signal with respect to the allocentric reference frame despite intact intrinsic HD tuning.

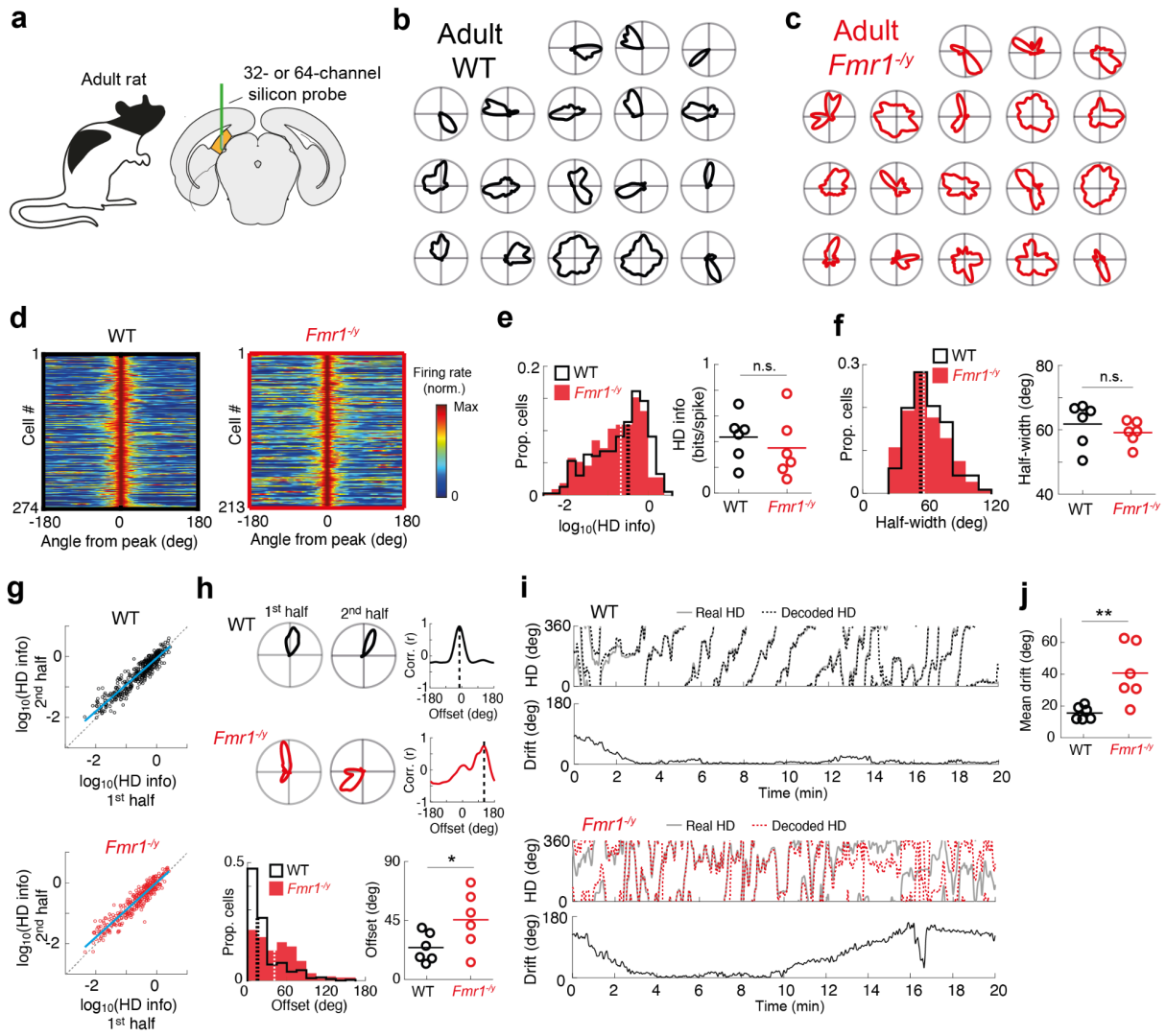

Figure 3. Normal HD tuning but degraded HD signal stability in adult *Fmr1*$^{-/y}$ rats. a, silicon probe placement in PoSub. **b**,**c**, example tuning curves of PoSub cells in adult WT (**b**) and *Fmr1*$^{-/y}$ rats (**c**). **d**, normalized HD tuning curves of PoSub cells with tuning curve width of less than 120 deg. **e**, **f**, overall distribution (left) and animal averages (right) of HD info (**e**) and tuning curve width (**f**) indicate normal levels of overall HD tuning in adults *Fmr1*$^{-/y}$ rats (HD info, LME: no genotype effect, $P > 0.05$; half-width, LME: no genotype effect, $P > 0.05$). **g**, Degree of HD tuning in PoSub cell tuning curves is preserved between two halves of an exploration epoch, indicating stable tuning fidelity (WT, $r = 0.94$, $P < 10^{-182}$; *Fmr1*$^{-/y}$, $r = 0.94$, $P < 10^{-158}$). Blue lines, linear fits. **h**, top, examples of HD tuning curves for two halves of a recording epoch and associated tuning cross-correlograms, showing considerable drift in a PoSub cell from an *Fmr1*$^{-/y}$ rat but stable firing direction for a PoSub cell in a WT rat. Dashed lines indicate the angular offset of maximum tuning curve correlation. Bottom, Overall distribution and animal averages of tuning curve offsets between two halves of the exploration epoch (angular offset between tuning curves, LME: genotype effect, $P < 0.05$). **i**, example real and decoded HD during a single recording session in WT and *Fmr1*$^{-/y}$ rats, as well as the low-pass drift of the decoded HD with respect to the animal's real HD. **j**, average drift of the HD signal across all recording sessions (t-test on animal averages: $t(10) = 3.33$, $P < 0.01$). Dashed lines on histograms, population medians; horizontal lines on animal average panels, means of animal averages.

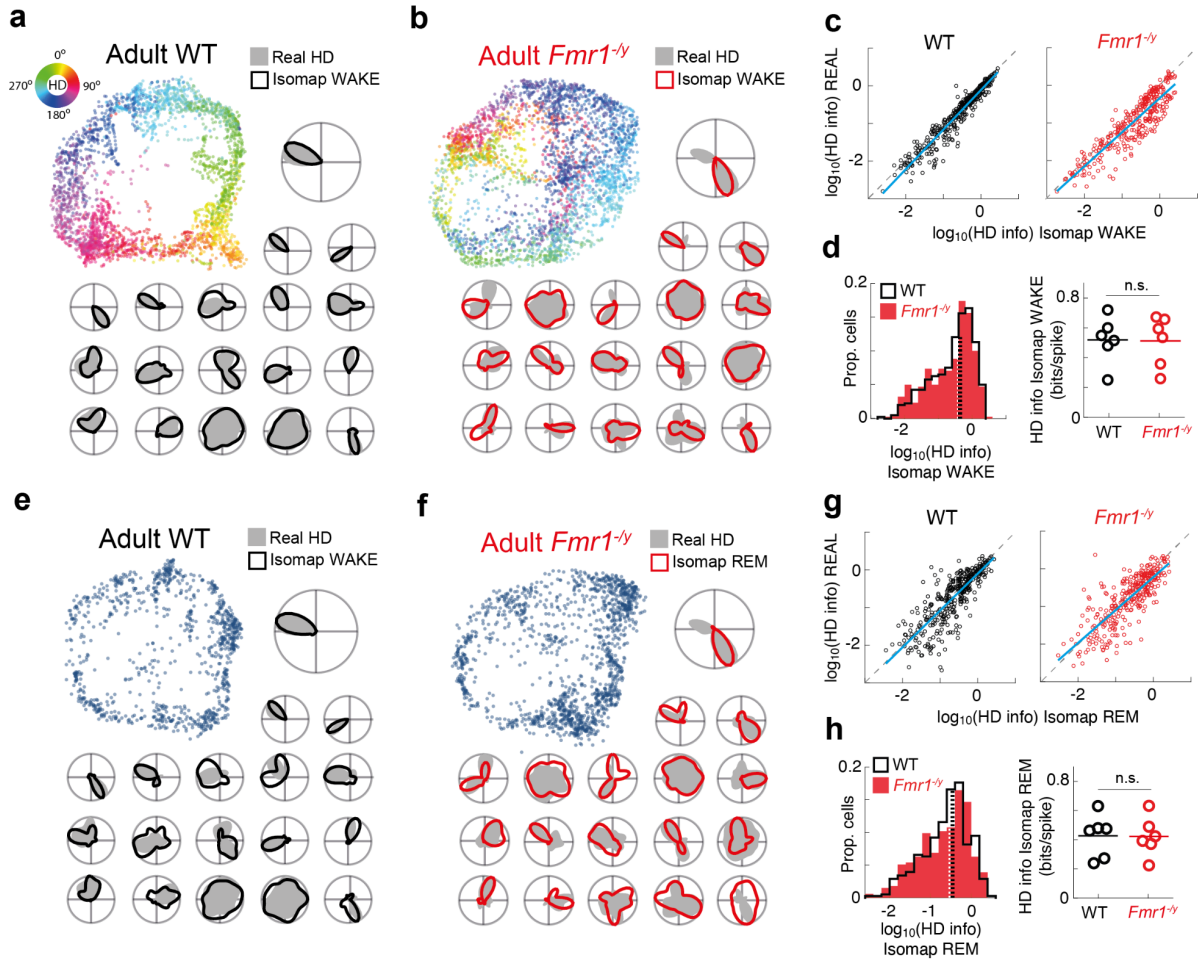

Figure 4. PoSub cells in adult *Fmr1*$^{-/y}$ rats show WT-like tuning to the internally generated HD signal. **a**, **b**, Example Isomap projections of PoSub cell population vectors during WAKE in adult WT rats (**a**) and *Fmr1*$^{-/y}$ rats (**b**). While real HD tuning curves in *Fmr1*$^{-/y}$ rats show signs of drift, HD tuning curves reconstructed from the Isomap projection are not contaminated by drift since they rely on the internal representation of HD. The mapping of real HD onto the manifold is more diffuse in *Fmr1*$^{-/y}$ rats, indicating drift of the internal HD with respect to the allocentric reference frame. **c**, Amount of HD tuning in PoSub cells is preserved in the tuning curves reconstructed from population activity during WAKE (WT, $r = 0.95$, $P < 10^{-208}$; *Fmr1*$^{-/y}$, $r = 0.90$, $P < 10^{-120}$). Blue lines, linear fits. **d**, overall distribution (left) and animal averages (right) of HD info indicate normal levels of HD tuning in juvenile *Fmr1*$^{-/y}$ rats when measured independently of any reference frames (LME: no genotype effect, $P > 0.05$). **e**, **f**, Example Isomap projections of PoSub population vectors during REM sleep from the same recording sessions as in **a** and **b**. **g**, HD tuning in PoSub cells is preserved in REM (WT, $r = 0.82$, $P < 10^{-93}$; *Fmr1*$^{-/y}$, $r = 0.80$, $P < 10^{-74}$). Blue lines, linear fits. **h**, overall distribution (left) and animal averages (right) of HD info indicate normal levels of HD tuning in adult *Fmr1*$^{-/y}$ rats during REM (LME: no genotype effect, $P > 0.05$). Dashed lines on histograms, population medians; horizontal lines on animal average panels, means of animal averages.

Discussion

In the present study, we leveraged the experimental tractability of the cortical HD system [23,26,29,30] in *Fmr1*$^{-/y}$ rats to reveal an unexpected enhancement of HD tuning in PoSub that is apparent at 3-4 weeks of age which disappears by adulthood. This phenotype was accompanied by an enhanced anchoring of the HD signal to the external world in juvenile *Fmr1*$^{-/y}$ rats. Reconstruction of the intrinsic HD tuning curves from PoSub cell activity manifolds during both wakefulness and REM sleep allowed us to dissociate these two phenomena and show that the enhanced fidelity of the HD signal in juvenile *Fmr1*$^{-/y}$ rats is independent of anchoring. On the other hand, upon reaching adulthood, the intrinsic HD signal in *Fmr1*$^{-/y}$ rats became more WT-like but its anchoring to the external world was compromised.

The tuning of HD cells in PoSub arises from sub-thalamic structures [35] and is thought to originate in the network comprising the dorsal tegmental nucleus (DTN) in the brainstem as well as the medial mammillary nucleus (LMN). Modeling [36–39] and lesion [40,41] studies indicate that directional firing fields of HD cells are a consequence of a highly structured connectivity patterns in the DTN-LMN network, whereby cells coding for similar directions inhibit cells that fire for opposite directions, likely via inhibitory interneurons. Such a ring attractor network can support an activity packet independently of brain states, which is in line with the observations that a coherent HD signal can be decoded during sleep [26,29]. The exact connectivity within this network can determine the width of this activity packet and thus the tuning of individual HD cells. Thus, one possibility is that the transient enhancement of cortical HD tuning observed in juvenile *Fmr1*$^{-/y}$ rats is a consequence of altered connectivity in the LMN-DTN circuit and/or in projections from this circuit, via the anterior dorsal thalamic nucleus (ADN) to PoSub; further experiments are necessary to determine whether there are alterations in HD coding in these upstream structures.

On the other hand, the HD signal is thought to be anchored to the external world through top-down cortical projections to PoSub [42]. Vision is the primary modality for this process, and the information about stable visual landmarks may reach PoSub either directly from the primary visual cortex or via prominent inputs from the retrosplenial cortex [43], where a subset of neurons are selective for visual landmarks [44,45]. Thus, it is conceivable that in juvenile *Fmr1*$^{-/y}$ rats, two separate processes are enhanced, likely independently of each other: the subcortical generation of the intrinsic HD signal and/or its transmission to the cortex, as well as the cortically-driven anchoring of the HD signal to the external world. Still, the exact sensory modality mediating the latter phenotype is to be determined, and another possibility is that juvenile *Fmr1*$^{-/y}$ rats enhance their anchoring by more efficient use of the olfactory [46], or somatosensory [22] systems.

The independence of these two processes is further supported by our finding that in adult *Fmr1*$^{-/y}$ rats the intrinsic HD signal is intact across both wakefulness and sleep, but its anchoring to the external world is disrupted. An intact HD signal that is not correctly anchored to the allocentric reference frame is present in very young juvenile rats (P10-P14) prior to eye opening [22], and in adult rodents it detaches from the external world whenever the visual inputs are compromised [46]. In P12-P14 rats, this anchoring deficit can be mitigated by providing polarising somatosensory information. It is thus possible that adult *Fmr1*$^{-/y}$ rats have a sensory deficit that interferes with the correct mapping of the internal HD to the allocentric reference frame. This deficit could include alterations in processing or integration of external sensory information (such as visual, olfactory or tactile landmarks in the environment) and/or processing or integration of self motion cues (such

as angular velocity, optic flow and motor efference copy) all of which can be used to update the HD signal as the animal moves around within the environment.

The phenotypes we observed in juvenile (P22-26) and adult *Fmr1*$^{-/y}$ rats appear to be independent and to have arisen due to neuronal alterations at different stages of information processing. The deficient anchoring of the HD signal to the external world only emerged during later postnatal development or during adulthood, which is reminiscent of developmental regression which is sometimes observed in children with autism. During developmental regression, already acquired skills are lost, usually around the 2nd and 3rd year of life [47]. Several studies have shown that some later-emerging *Fmr1*$^{-/y}$ phenotypes arise as secondary adaptations to the direct effects of FMRP's absence on the level of cellular excitability [48–50]. Thus, the age-specific differences seen in HD coding and stability in *Fmr1*$^{-/y}$ rats might arise as imperfect homeostatic adaptations to direct effects of lack of FMRP, but further research is needed to elucidate how this might occur on a systems level.

Methods

Animals

All experimental procedures were carried out under a UK Home Office project licence, approved by the Animal Welfare and Ethical Review Board (AWERB) of the University of Edinburgh College of Medicine and Veterinary Medicine, and conformed with the UK Animals (Scientific Procedures) Act 1986. Long-Evans male *Fmr1*$^{-/y}$ and WT rat littermates were bred in-house by crossing WT sires with *Fmr1*-heterozygous dams. The original null mutants were generated using zinc finger nucleases targeting *Fmr1* exon 1 with a construct containing the sequence coding for eGFP. The *Fmr1*$^{-/y}$ males from the resulting line do not express either FMRP or eGFP, as described in [4]. The rats used for the experiments described in this thesis were bred in-house and were housed with their parents and siblings up until weaning at postnatal day 21 (P21). After weaning, animals were housed with their littermates. They were kept on a 12h/12h light/dark cycle (lights on at 7am) and fed ad libitum on standard laboratory chow, with supplementation of water-soaked breeding chow after the surgery. 24 hours after the end of the surgery, adult rats were placed on mild food restriction to encourage foraging, with their body weight not falling below 90% of their free feeding weight. Pairs of rats (i.e. 1 WT and 1 *Fmr1*$^{-/y}$ rat) were randomly allocated to the experiment from the litter. Experimenters were blind to the genotype of the animals chosen throughout experiments including surgery, recordings, and pre-processing, and were unblinded to conduct statistical comparisons between groups.

Surgery

Rats were anaesthetised using 1.5-3.5% isoflurane, while the animal's respiratory rate and heart rate were monitored using a PhysioSuite box (Kent Scientific) and their body heat was maintained at 37° using a homeothermic blanket system (Harvard Apparatus). 0.08ml of rimadyl (50mg/ml carprofen) was given per kg of bodyweight shortly after induction of anaesthesia. To secure the headcap and implant on the head, the skull was covered with dental adhesive (Optibond Universal). In adults, this was supplemented with three to five self-tapping jeweller's screws. A silver ground wire was placed directly above the cerebellum in juveniles or attached to one of the

skull screws placed above the cerebellum in adult rats. A craniotomy was drilled over the left postsubiculum, and a silicon probe (Cambridge Neurotech, models H5, H6b or H7) was lowered into the brain, slightly above the target area (juveniles, from Bregma: anterior-posterior (AP), −6.30 mm; medial-lateral (ML), 3.10 mm; dorsal-ventral (DV), −1.60 mm; adults, from Bregma: AP, −7.64 mm; ML, 3.30 mm; DV, −1.70 mm). The silicon probe was mounted on a drive (3DNeuro or made in-house), secured onto the skull's surface using dental acrylic. After surgery, the animals were allowed to recover on a heated bench (30°C) for at least one hour and returned to the animal house for at least 24 hours before recording. Juvenile rats were single-housed after surgery, and adults were single-housed or housed with a sibling in a cage with a divider separating them. Juvenile rats were implanted between postnatal days 20-23 (P20-P23), and adult rats were at least 7 weeks old at the time of implantation.

Recording

Silicon probes were initially implanted into the white matter above PoSub and were advanced into PoSub in 30 µm increments 24-48h after surgery until spiking activity could be seen on all channels. Tissue was allowed to settle for at least 3 h before recordings commenced. If the tip of the probe wasl within PoSub, the probe was advanced further in the end of the recording session until the tip reached the pia mater and another recording was performed on subsequent day. In all cases probe tracts were confirmed histologically to pass through PoSub (Figure S1d, Figure S2d), and in all cases the probe reached the pial surface of PoSub by the last recording. The recording environment consisted of a cylindrical arena of 73 cm diameter, with 54 cm tall walls, painted light blue. A prominent visual cue was positioned at the top of the wall on the north side; this was 31.5 cm wide and 26 cm tall and consisted of two black horizontal stripes with a white stripe between them. The rat was taken within the curtains surrounding the recording enclosure and plugged in. It was then placed within the cylindrical arena from the south side, Coco Pops cereals (Kellogg's) were scattered on the floor and the rat was left to forage and explore for 20 min. After that, the rat was given a 90-minute sleep opportunity in a container placed inside the recording arena, during which recordings continued. The arena was swept and cleaned with chlorhexidine (Vetasept) spray between the exploration and sleep sessions. On recording days, the rat was always introduced into the arena from the south.

For recording, the implanted silicon probe was connected to an Intan RHD headstage (Intan technologies). The headstage was connected to an Intan RHD standard SPI cable, which was connected to a 3D-printed commutator in the ceiling (custom-made in house). Signals were acquired at 30kHz with an OpenEphys data acquisition system. For tracking the rat's position and head direction, a bright red and a bright green marker were attached on the right and left of the headstage. Video capturing and marker tracking were performed using Bonsai software [51] at 40 Hz. For the juvenile recordings, images were acquired through a Logitech C930e camera. To synchronise the images with the electrophysiology data, an Arduino microcontroller was programmed to send a random sequence of pulses to both the OpenEphys system and a LED light within the frame of the camera. The times when the LED light shone were detected by Bonsai and synchronisation of the pulses in the light and the electrophysiology data was done offline. For the adult recordings, images were acquired through an acA1300-75gc Basler camera with a LMVZ4411 Kowa lens, positioned at the ceiling of the rig. This camera was connected to the

OpenEphys board, sending a pulse for each frame taken, allowing the synchronisation of the two streams of information.

Perfusion and probe recovery

After the end of data gathering, the rats were anaesthetised with 5% isoflurane and injected intraperitoneally with a lethal dose of pentobarbitone (≥1ml for adults and ≥ 0.3ml for juvenile rats). After their reflexes were gone, they underwent transcardial perfusion first with 0.9% saline, until the liver started turning pale, and then 4% formalin or paraformaldehyde solution. Then the probe was retracted from the brain, and was kept moist by dropping distilled water using a Pasteur pipette regularly. The rat was decapitated and the brain extracted. Then, the probe and drive complex was carefully recovered from the skull and headcap. After recovery, the probe was dipped in and out of a 1:5 solution of Contrad 70 liquid detergent in distilled water heated to roughly 60°C for 5 minutes, twice. After that, the probe was left to soak in a 1-2% fresh solution of tergazyme detergent, and finally another 5-minute round of dips in hot Contrad was repeated. The probe was then rinsed with distilled water, and channel impedances were measured in 0.9% saline using the OpenEphys system. If the recording quality of the previous rat was good and the impedance values were satisfactory (most channels <0.5MOhm), the probe was reimplanted in the next rat.

Spike sorting and cell classification

Spikes were first sorted automatically into clusters using Kilosort 2.0 (Pachitariu et al., 2016). Then, manual curation was performed while visualising the automatically created clusters on Klusters software. At this stage, any cluster without a clear waveform and clear dip in the spike train autocorrelogram at the 0-1 ms time bin was classified as noise and cluster pairs with similar waveforms and a clear dip in their spike train cross-correlograms at the 0-1 ms time bin were merged. Viable units were first identified as units that had a waveform with negative deflection (criterion aiming to exclude spikes from fibers of passage). Next, a cluster contamination score was computed from the spike autocorrelograms, as a ratio of the amplitudes of the 0-1 ms bin and the maximum amplitude within 0-100 ms. Units with cluster contamination scores below 0.5 were excluded from the analysis. Next, putative excitatory cells were classified on the basis of trough-to-peak duration of their average waveforms. The threshold was based on the trough of the bimodal distribution of trough-to-peak durations and was set at > 0.5 ms for juvenile rats and > 0.4 ms for adult rats. Since mean firing rate of PoSub cells is highly dependent on the width of the tuning HD tuning, we minimised the bias towards broadly tuned cells by only excluding cells that fired less than 100 spikes in a given epoch. In order to prevent double-counting of recorded cells, we also excluded any cells recorded in the portion of PoSub that had already been recorded on the previous day, except for population-based analyses that rely on simultaneously recorded assemblies.

HD tuning curves

The animal's HD was calculated based on the line perpendicular to the line connecting the red and green markers attached to the headcap. Periods with more than 1 second without viable tracking data were excluded from the analysis. HD tuning curves were then computed as the ratio between histograms of spike count and total time spent in each direction in bins of 1° and

smoothed with a Gaussian kernel of 6° SD, except for Isomap analyses where tuning curves were computed in 6° bins (with 12° SD Gaussian kernel) to account for relatively short duration of REM sleep episodes in adult rats. Tuning curves were computed from epochs when the animal's speed exceeded 1 cm/s for all analyses except Bayesian decoding and Isomap analyses, where the threshold was set to 2 cm/s.

The half-width of the HD tuning curves was computed by first finding the bin with the highest firing rate, and then averaging the two sides of the tuning curve. Half-width was then defined as twice the angular distance between the maximal firing rate and the half-maximal firing rate of the resulting half of the tuning curve. HD information contained in the tuning curves calculated for N angular bins as:

$$I = \sum_{i=1..N} \lambda(\Theta_i)\, log_2\left(\frac{\lambda(\Theta_i)}{\lambda}\right) p(\Theta_i)$$

where $\lambda(\Theta_i)$ is the firing rate of the cell for the *i*th angular bin, λ is the average firing rate of the neuron during exploration and $p(\Theta_i)$ is the occupancy (i.e. normalized time spent) in direction Θ_i.

We obtained HD tuning curve cross-correlograms by computing Pearson's correlation coefficients between the reference tuning curve vector and the second tuning curve vector (from either the same or another cell), which was circularly shifted by 1 to maximum number of bins.

Classification of sleep states

Sleep scoring was performed using the automated SleepScoreMaster algorithm and TheStateEditor software (Buzsaki laboratory, https://github.com/buzsakilab). The wide-band signal was downsampled to 1.25 kHz and used as the LFP signal. Electromyograph (EMG) was computed from correlated high-frequency noise across several channels of the linear probe.

Visualization and analysis of the population manifold

For visualization of the PoSub manifold, cell spike times from the whole epoch were binned into population vectors in 200 ms bins, smoothened in 400 ms SD Gaussian windows and a square root of each value was taken. The resulting population vectors were then z-scored in the time domain, and each vector was divided by its norm. In order to account for the differences in the number of cells recorded in each session, we projected population vectors into a feature space using kernel PCA with a Laplacian kernel. Six PCs that explained the most variance were input into the Isometric Feature Mapping (Isomap) algorithm implemented in the Matlab Toolbox for Dimensionality Reduction Reduction (version 0.8.1b, https://lvdmaaten.github.io/drtoolbox/). The parameters were set to 30 nearest neighbours and 2 dimensions.

Virtual HD at each time bin was then calculated as a four-quadrant arctangent of the two Isomap dimensions (range: -180° to 180°). Importantly, the internal HD generated this way has arbitrary directionality (clockwise/anticlockwise) and an arbitrary point of origin. To align it, Isomap directionality was established by computing the Isomap error as the difference between real HD values and (1) internal HD values and (2) internal HD multiplied by -1 and selecting the directionality with the error of smallest circular variance. Internal HD tuning curves were then computed as the ratio between histograms of spike count and total time spent in each internal HD

in bins of 6 degrees and smoothed with a Gaussian kernel of 12° SD. Real HD tuning curves for comparison with Isomap tuning curves were computed by downsampling the real HD into 200ms bins and applying the same procedure as above. In order to correct for the arbitrary point of origin, HD tuning curve cross-correlations (see above) were computed between each real and internal HD tuning curve of each HD cell, and the offset of maximum correlation was then used to circularly shift tuning curve vectors by the equivalent number of bins.

Data analysis and statistics

All analyses were conducted using Matlab R2020b (Mathworks) with TStoolbox 2.0 and Circular Statistics Toolbox version 1.2167. Statistical comparisons of individual cell data were performed using a generalized linear mixed model (GLMM) approach in order to take into account the hierarchy of dependency in our data sets (genotypes-rats-neurons) and account for random effects. Statistical modelling routines for the linear mixed effects (LME) models were written and run using RStudio 2023.12. (RStudio Team). Depending on the data distribution, linear mixed models (LMMs) or generalized linear mixed models (GLMMs) were fitted to single unit data metrics using the R package lme4 v1.1–17. Animal and cell identity were included in models as random effects, and genotypes were included as fixed effects. Terms are progressively eliminated when a simpler model (i.e. a model not containing that term) fits the data equally well (based on likelihood ratio test). Consequently, the p-values reported in the context of LMEs are given by likelihood ratio tests between a model containing the variable or interaction in question and a model without that variable or interaction (a reduced/null model). All statistically significant differences obtained through LMEs were also statistically significant when comparisons were made using a two-sample Mann-Whitney U test with cells as experimental units.

Statistical comparisons on animal averages (where stated) were performed with independent Student's t-tests. All statistical tests are two-tailed. No statistical methods were used to pre-determine sample sizes but our sample sizes are similar to those reported in previous publications.

Data Availability

Data will be made openly available at the time of publication.

Code Availability

Code will be made openly available at the time of publication.

Acknowledgements

NM was supported by a PhD studentship from the Simons Initiative for the Developing Brain. This work was supported by pilot funding from the Edinburgh-McGill pilot funding scheme (AP, ERW), a Simons Initiative for the Developing Brain grant (ERW & AA), the Simons Foundation Autism Research Initiative grant AN-AR-Rat Models-0090333 (AJD, PAD, and AP), the Canadian Research Chair in Systems Neuroscience (AP), CIHR Project Grants 155957 and 180330 (AP); NSERC Discovery Grant RGPIN-2018-04600 (AP).

The authors thank Lynn Morrison and the other animal technicians from the University of Edinburgh George Square Bioveterinary Services Facility for their expertise & assistance in this work, and Dr Owen Dando for help implementing the LME analysis.

Declaration of Interests

Authors declare no competing interests in relation to this work.

Bibliography

1. Manoli, D.S., and State, M.W. (2021). Autism Spectrum Disorder Genetics and the Search for Pathological Mechanisms. Am. J. Psychiatry *178*, 30–38. https://doi.org/10.1176/appi.ajp.2020.20111608.
2. Möhrle, D., Fernández, M., Peñagarikano, O., Frick, A., Allman, B., and Schmid, S. (2020). What we can learn from a genetic rodent model about autism. Neurosci. Biobehav. Rev. *109*, 29–53. https://doi.org/10.1016/j.neubiorev.2019.12.015.
3. Till, S.M., Asiminas, A., Jackson, A.D., Katsanevaki, D., Barnes, S.A., Osterweil, E.K., Bear, M.F., Chattarji, S., Wood, E.R., Wyllie, D.J.A., et al. (2015). Conserved hippocampal cellular pathophysiology but distinct behavioural deficits in a new rat model of FXS. Hum. Mol. Genet. *24*, 5977–5984. https://doi.org/10.1093/hmg/ddv299.
4. Asiminas, A., Jackson, A.D., Louros, S.R., Till, S.M., Spano, T., Dando, O., Bear, M.F., Chattarji, S., Hardingham, G.E., Osterweil, E.K., et al. (2019). Sustained correction of associative learning deficits after brief, early treatment in a rat model of Fragile X Syndrome. Sci. Transl. Med. *11*, eaao0498. https://doi.org/10.1126/scitranslmed.aao0498.
5. Asiminas, A., Booker, S.A., Dando, O.R., Kozic, Z., Arkell, D., Inkpen, F.H., Sumera, A., Akyel, I., Kind, P.C., and Wood, E.R. (2022). Experience-dependent changes in hippocampal spatial activity and hippocampal circuit function are disrupted in a rat model of Fragile X Syndrome. Mol. Autism *13*, 49. https://doi.org/10.1186/s13229-022-00528-z.
6. Katsanevaki, D., Till, S., Buller-Peralta, I., Watson, T., Nawaz, M., Arkell, D., Tiwari, S., Kapgal, V., Biswal, S., Smith, J., et al. (2020). Heterozygous deletion of SYNGAP enzymatic domains in rats causes selective learning, social and seizure phenotypes. Preprint at bioRxiv, https://doi.org/10.1101/2020.10.14.339192 https://doi.org/10.1101/2020.10.14.339192.
7. Katsanevaki, D., Till, S.M., Buller-Peralta, I., Nawaz, M.S., Louros, S.R., Kapgal, V., Tiwari, S., Walsh, D., Anstey, N.J., Petrović, N.G., et al. (2024). Key roles of C2/GAP domains in SYNGAP1-related pathophysiology. Cell Rep. *43*. https://doi.org/10.1016/j.celrep.2024.114733.
8. Klibaite, U., Li, T., Aldarondo, D., Akoad, J.F., Ölveczky, B.P., and Dunn, T.W. (2024). Mapping the landscape of social behavior. Preprint at bioRxiv, https://doi.org/10.1101/2024.09.27.615451 https://doi.org/10.1101/2024.09.27.615451.
9. Lim, H.K., Yoon, J.H., and Song, M. (2022). Autism Spectrum Disorder Genes: Disease-Related Networks and Compensatory Strategies. Front. Mol. Neurosci. *15*. https://doi.org/10.3389/fnmol.2022.922840.
10. Booker, S.A., Domanski, A.P.F., Dando, O.R., Jackson, A.D., Isaac, J.T.R., Hardingham, G.E., Wyllie, D.J.A., and Kind, P.C. (2019). Altered dendritic spine function and integration in a mouse model of fragile X syndrome. Nat. Commun. *10*, 4813. https://doi.org/10.1038/s41467-019-11891-6.
11. Domanski, A.P.F., Booker, S.A., Wyllie, D.J.A., Isaac, J.T.R., and Kind, P.C. (2019). Cellular and synaptic phenotypes lead to disrupted information processing in Fmr1-KO mouse layer 4 barrel cortex. Nat. Commun. *10*, 4814. https://doi.org/10.1038/s41467-019-12736-y.

12. Raspanti, A., Pizzo, R., Gurgone, A., Giraudo, C., Sagona, G., Macioce, A., Battaglia, A., Katsanou, L., Medici, G., Ferrini, F., et al. (2024). Postnatal Sensory Experience and Barrel Cortex Alterations Anticipate Autistic Traits in a Mouse Model of Cdkl5 Deficiency Disorder. Preprint at bioRxiv, https://doi.org/10.1101/2024.12.20.629347 https://doi.org/10.1101/2024.12.20.629347.
13. Fagiolini, M., Pizzorusso, T., Berardi, N., Domenici, L., and Maffei, L. (1994). Functional postnatal development of the rat primary visual cortex and the role of visual experience: dark rearing and monocular deprivation. Vision Res. *34*, 709–720. https://doi.org/10.1016/0042-6989(94)90210-0.
14. Mitrukhina, O., Suchkov, D., Khazipov, R., and Minlebaev, M. (2015). Imprecise Whisker Map in the Neonatal Rat Barrel Cortex. Cereb. Cortex N. Y. N 1991 *25*, 3458–3467. https://doi.org/10.1093/cercor/bhu169.
15. Che, A., Babij, R., Iannone, A.F., Fetcho, R.N., Ferrer, M., Liston, C., Fishell, G., and García, N.V.D.M. (2018). Layer I Interneurons Sharpen Sensory Maps during Neonatal Development. Neuron *99*, 98-116.e7. https://doi.org/10.1016/j.neuron.2018.06.002.
16. Ames, C., and Fletcher-Watson, S. (2010). A review of methods in the study of attention in autism. Dev. Rev. *30*, 52–73. https://doi.org/10.1016/j.dr.2009.12.003.
17. Robertson, C.E., and Baron-Cohen, S. (2017). Sensory perception in autism. Nat. Rev. Neurosci. *18*, 671–684. https://doi.org/10.1038/nrn.2017.112.
18. McNaughton, B.L., Battaglia, F.P., Jensen, O., Moser, E.I., and Moser, M.-B. (2006). Path integration and the neural basis of the “cognitive map.” Nat. Rev. Neurosci. *7*, 663–678. https://doi.org/10.1038/nrn1932.
19. Langston, R.F., Ainge, J.A., Couey, J.J., Canto, C.B., Bjerknes, T.L., Witter, M.P., Moser, E.I., and Moser, M.-B. (2010). Development of the Spatial Representation System in the Rat. Science.
20. Wills, T.J., Cacucci, F., Burgess, N., and O’Keefe, J. (2010). Development of the hippocampal cognitive map in preweanling rats. Science *328*, 1573–1576. https://doi.org/10.1126/science.1188224.
21. Tan, H.M., Bassett, J.P., O’Keefe, J., Cacucci, F., and Wills, T.J. (2015). The Development of the Head Direction System before Eye Opening in the Rat. Curr. Biol. *25*, 479–483. https://doi.org/10.1016/j.cub.2014.12.030.
22. Bassett, J.P., Wills, T.J., and Cacucci, F. (2018). Self-Organized Attractor Dynamics in the Developing Head Direction Circuit. Curr. Biol. *28*, 609-615.e3. https://doi.org/10.1016/j.cub.2018.01.010.
23. Chaudhuri, R., Gerçek, B., Pandey, B., Peyrache, A., and Fiete, I. (2019). The intrinsic attractor manifold and population dynamics of a canonical cognitive circuit across waking and sleep. Nat. Neurosci. *22*, 1512–1520. https://doi.org/10.1038/s41593-019-0460-x.
24. Gardner, R.J., Hermansen, E., Pachitariu, M., Burak, Y., Baas, N.A., Dunn, B.A., Moser, M.-B., and Moser, E.I. (2022). Toroidal topology of population activity in grid cells. Nature *602*, 123–128. https://doi.org/10.1038/s41586-021-04268-7.
25. Senzai, Y., and Scanziani, M. (2022). A cognitive process occurring during sleep is revealed by rapid eye movements. Science *377*, 999–1004. https://doi.org/10.1126/science.abp8852.
26. Duszkiewicz, A.J., Orhan, P., Skromne Carrasco, S., Brown, E.H., Owczarek, E., Vite, G.R., Wood, E.R., and Peyrache, A. (2024). Local origin of excitatory–inhibitory tuning equivalence in a cortical network. Nat. Neurosci. *27*, 782–792. https://doi.org/10.1038/s41593-024-01588-5.
27. Peng, J.-J., Throm, B., Jazi, M.N., Yen, T.-Y., Monyer, H., and Allen, K. (2023). Grid cells perform path integration in multiple reference frames during self-motion-based navigation. Preprint at bioRxiv, https://doi.org/10.1101/2023.12.21.572857 https://doi.org/10.1101/2023.12.21.572857.
28. Hermansen, E., Klindt, D.A., and Dunn, B.A. (2024). Uncovering 2-D toroidal

representations in grid cell ensemble activity during 1-D behavior. Nat. Commun. *15*, 5429. https://doi.org/10.1038/s41467-024-49703-1.
29. Peyrache, A., Lacroix, M.M., Petersen, P.C., and Buzsáki, G. (2015). Internally organized mechanisms of the head direction sense. Nat. Neurosci. *18*, 569–575. https://doi.org/10.1038/nn.3968.
30. Taube, J.S., Muller, R.U., and Ranck, J.B. (1990). Head-direction cells recorded from the postsubiculum in freely moving rats. I. Description and quantitative analysis. J. Neurosci. *10*, 420–435. https://doi.org/10.1523/JNEUROSCI.10-02-00420.1990.
31. Taube, J.S. (2007). The Head Direction Signal: Origins and Sensory-Motor Integration. Annu. Rev. Neurosci. *30*, 181–207. https://doi.org/10.1146/annurev.neuro.29.051605.112854.
32. Hunter, J., Rivero-Arias, O., Angelov, A., Kim, E., Fotheringham, I., and Leal, J. (2014). Epidemiology of fragile X syndrome: a systematic review and meta-analysis. Am. J. Med. Genet. A. *164A*, 1648–1658. https://doi.org/10.1002/ajmg.a.36511.
33. Yu, Z., Guindani, M., Grieco, S.F., Chen, L., Holmes, T.C., and Xu, X. (2022). Beyond t test and ANOVA: applications of mixed-effects models for more rigorous statistical analysis in neuroscience research. Neuron *110*, 21–35. https://doi.org/10.1016/j.neuron.2021.10.030.
34. Rybakken, E., Baas, N., and Dunn, B. (2019). Decoding of Neural Data Using Cohomological Feature Extraction. Neural Comput. *31*, 68–93. https://doi.org/10.1162/neco_a_01150.
35. Goodridge, J.P., and Taube, J.S. (1997). Interaction between the Postsubiculum and Anterior Thalamus in the Generation of Head Direction Cell Activity. J. Neurosci. *17*, 9315–9330. https://doi.org/10.1523/JNEUROSCI.17-23-09315.1997.
36. Skaggs, W.E., Knierim, J.J., Kudrimoti, H.S., and McNaughton, B.L. (1995). A model of the neural basis of the rat's sense of direction. Adv. Neural Inf. Process. Syst. *7*, 173–180.
37. Redish, A.D., Elga, A.N., and Touretzky, D.S. (1996). A coupled attractor model of the rodent Head Direction system. Netw. Comput. Neural Syst. *7*, 671–685. https://doi.org/10.1088/0954-898X_7_4_004.
38. Sharp, P.E., Blair, H.T., and Cho, J. (2001). The anatomical and computational basis of the rat head-direction cell signal. Trends Neurosci. *24*, 289–294. https://doi.org/10.1016/s0166-2236(00)01797-5.
39. Xie, X., Hahnloser, R.H.R., and Seung, H.S. (2002). Double-ring network model of the head-direction system. Phys. Rev. E *66*, 041902. https://doi.org/10.1103/PhysRevE.66.041902.
40. Blair, H.T., Cho, J., and Sharp, P.E. (1998). Role of the lateral mammillary nucleus in the rat head direction circuit: a combined single unit recording and lesion study. Neuron *21*, 1387–1397. https://doi.org/10.1016/s0896-6273(00)80657-1.
41. Bassett, J.P., Tullman, M.L., and Taube, J.S. (2007). Lesions of the tegmentomammillary circuit in the head direction system disrupt the head direction signal in the anterior thalamus. J. Neurosci. Off. J. Soc. Neurosci. *27*, 7564–7577. https://doi.org/10.1523/JNEUROSCI.0268-07.2007.
42. Yoder, R.M., Clark, B.J., and Taube, J.S. (2011). Origins of landmark encoding in the brain. Trends Neurosci. *34*, 561–571. https://doi.org/10.1016/j.tins.2011.08.004.
43. Richevaux, L., Lim, D., Nassar, M., Rodrigues, L.D., Mauthe, C., Cohen, I., Sol-Foulon, N., and Fricker, D. (2023). Projection-specific integration of convergent thalamic and retrosplenial signals in the presubicular head direction cortex. eLife *12*. https://doi.org/10.7554/eLife.92443.1.
44. Jacob, P.-Y., Casali, G., Spieser, L., Page, H., Overington, D., and Jeffery, K. (2017). An independent, landmark-dominated head-direction signal in dysgranular retrosplenial cortex. Nat. Neurosci. *20*, 173–175. https://doi.org/10.1038/nn.4465.
45. Sit, K.K., and Goard, M.J. (2023). Coregistration of heading to visual cues in retrosplenial cortex. Nat. Commun. *14*, 1992. https://doi.org/10.1038/s41467-023-37704-5.

46. Asumbisa, K., Peyrache, A., and Trenholm, S. (2022). Flexible cue anchoring strategies enable stable head direction coding in both sighted and blind animals. Nat. Commun. *13*, 5483. https://doi.org/10.1038/s41467-022-33204-0.
47. Rogers, S.J. (2004). Developmental regression in autism spectrum disorders. Ment. Retard. Dev. Disabil. Res. Rev. *10*, 139–143. https://doi.org/10.1002/mrdd.20027.
48. Antoine, M.W., Langberg, T., Schnepel, P., and Feldman, D.E. (2019). Increased Excitation-Inhibition Ratio Stabilizes Synapse and Circuit Excitability in Four Autism Mouse Models. Neuron *101*, 648-661.e4. https://doi.org/10.1016/j.neuron.2018.12.026.
49. Domanski, A.P.F., Booker, S.A., Wyllie, D.J.A., Isaac, J.T.R., and Kind, P.C. (2019). Cellular and synaptic phenotypes lead to disrupted information processing in Fmr1-KO mouse layer 4 barrel cortex. Nat. Commun. *10*, 4814. https://doi.org/10.1038/s41467-019-12736-y.
50. Liu, X., Kumar, V., Tsai, N.-P., and Auerbach, B.D. (2022). Hyperexcitability and Homeostasis in Fragile X Syndrome. Front. Mol. Neurosci. *14*, 805929. https://doi.org/10.3389/fnmol.2021.805929.
51. Lopes, G., Bonacchi, N., Frazão, J., Neto, J.P., Atallah, B.V., Soares, S., Moreira, L., Matias, S., Itskov, P.M., Correia, P.A., et al. (2015). Bonsai: an event-based framework for processing and controlling data streams. Front. Neuroinformatics *9*, 7. https://doi.org/10.3389/fninf.2015.00007.

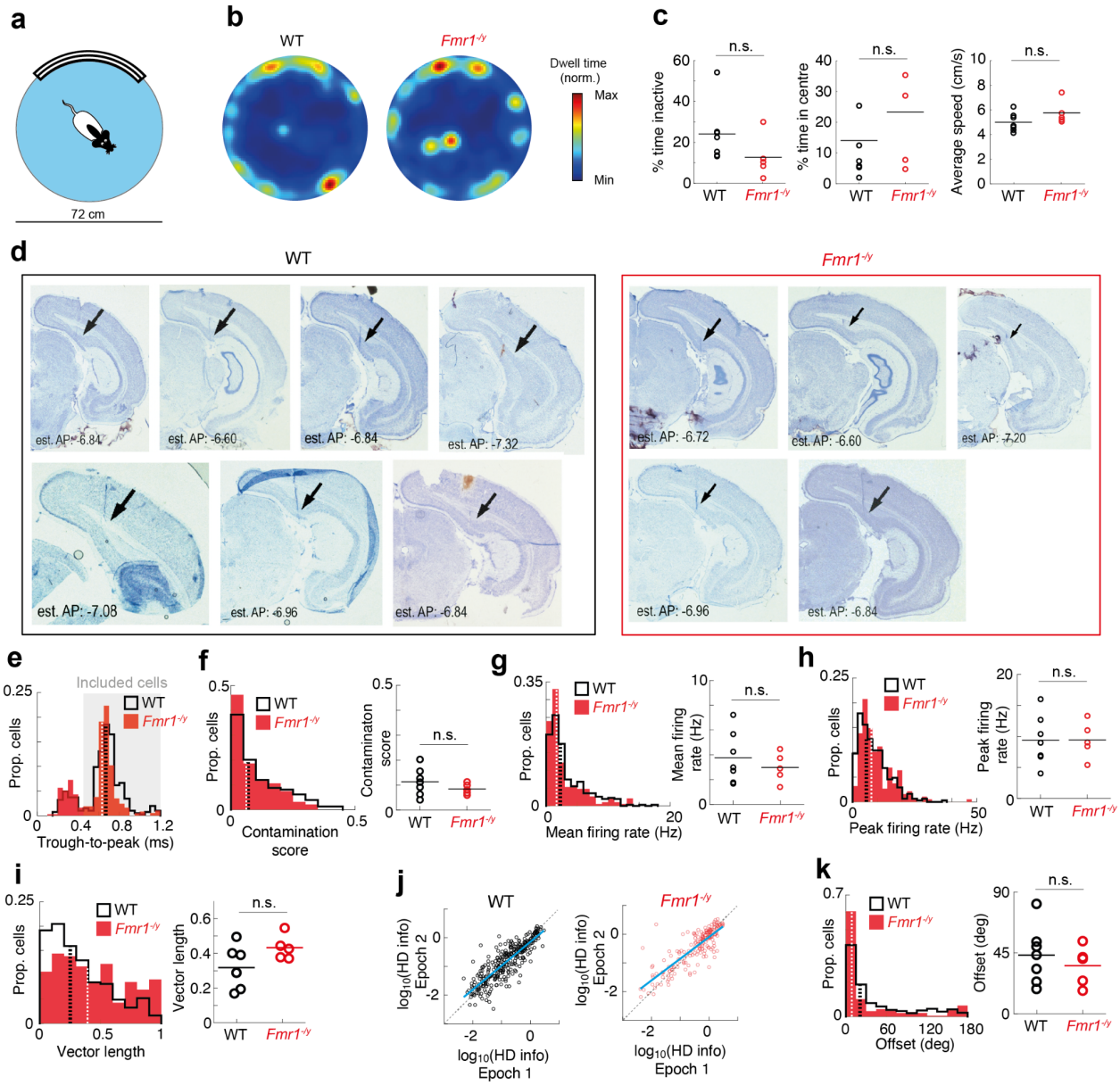

Figure S1. Behaviour, histology and single-cell metrics in juvenile rats. a, recording arena. **b**, heat maps of average occupancy across the two genotypes. **c**, percentage of time spent inactive (left; t-test on animal averages: t(10) = 1.53, $P > 0.05$) and in the centre of the arena (middle; t-test on animal averages: t(10) = 1.07, $P > 0.05$), and the average speed within the active period (right; t-test on animal averages: t(10) = 1.53, $P > 0.05$). **d**, silicon probe tracts going through PoSub, as visualized by Nissl staining. Black arrows, electrode tracts. **e**, distribution of the through-to-peak duration of all recorded units. Shaded area, cells classified as putative excitatory cells based on the trough in the bimodal distribution. **f**, cluster contamination scores across the two groups (LME: no genotype effect, $P > 0.05$). **g**,**h**, mean firing rates (LME: no genotype effect, $P > 0.05$) (**g**) and peak firing rates (**h**) of PoSub cells (LME: no genotype effect, $P > 0.05$). **i**, resultant vector length across the genotypes (LME: no genotype effect, $P > 0.05$). **j**, HD tuning is preserved across the two exploration epochs in both genotypes (WT, $r = 0.85$, $P < 10^{-64}$; *Fmr1-/y*, $r = 0.85$, $P < 10^{-87}$). **k**, drift of HD cell receptive fields across the two recording epochs (LME: no genotype effect, $P > 0.05$).

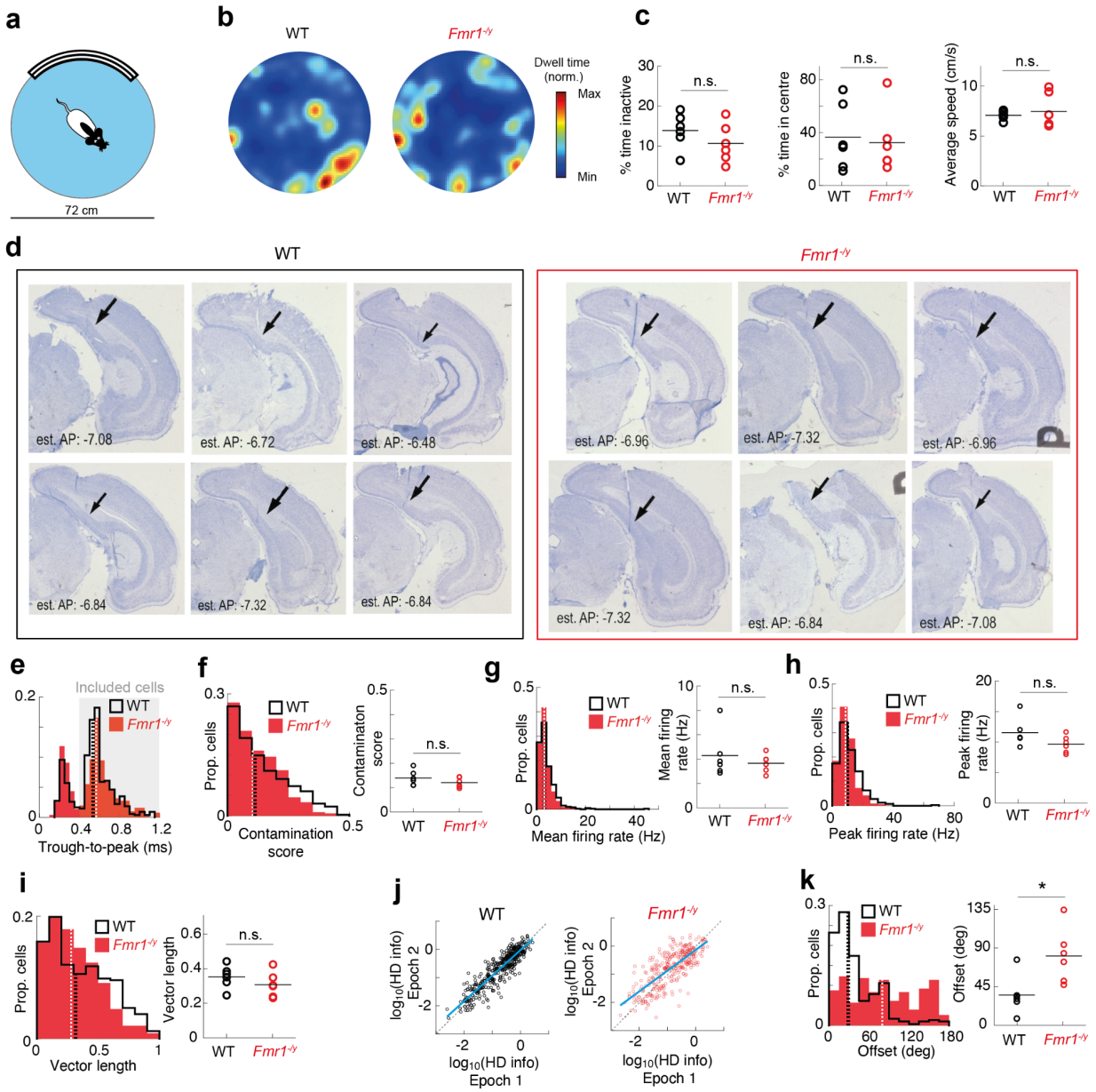

Figure S2. Behaviour, histology and single-cell metrics in adult rats. a, the same circular recording arena as the one used in juvenile rats. **b**, heat maps of average occupancy across the two genotypes. **c**, percentage of time spent inactive (left; t-test on animal averages: t(10) = 1.21, $P > 0.05$) and in the centre of the arena (middle; t-test on animal averages: t(10) = 0.29, $P > 0.05$), and the average speed within the active period (right; t-test on animal averages: t(10) = 0.51, $P > 0.05$). **d**, silicon probe tracts going through PoSub, as visualized by Nissl staining. Black arrows, electrode tracts. **e**, distribution of the through-to-peak duration of all recorded units. Shaded area, cells classified as putative excitatory cells based on the trough in the bimodal distribution. **f**, cluster contamination scores across the two groups (LME: no genotype effect, $P > 0.05$). **g**,**h**, mean firing rates (**g;** LME: no genotype effect, $P > 0.05$) and peak firing rates (**h;** LME: no genotype effect, $P > 0.05$) of PoSub cells. **i**, resultant vector length across the genotypes (LME: no genotype effect, $P > 0.05$). **j**, the quality of HD tuning is preserved across the two exploration epochs in both genotypes (WT, $r = 0.90$, $P < 10^{-145}$; *Fmr1-/y*, $r = 0.76$, $P < 10^{-61}$). **k**, drift of HD cell receptive fields across the two recording epochs (LME: genotype effect, $P < 0.05$).